

See discussions, stats, and author profiles for this publication at: <https://www.researchgate.net/publication/228357982>

Tailored Anatase/Brookite Nanocrystalline TiO₂. The Optimal Particle Features for Liquid- and Gas-Phase Photocatalytic Reactions

ARTICLE *in* THE JOURNAL OF PHYSICAL CHEMISTRY C · SEPTEMBER 2007

Impact Factor: 4.77 · DOI: 10.1021/jp0741096

CITATIONS

111

READS

49

6 AUTHORS, INCLUDING:



Claudia L. Bianchi

University of Milan

213 PUBLICATIONS 4,004 CITATIONS

SEE PROFILE



Carlo Pirola

University of Milan

94 PUBLICATIONS 1,036 CITATIONS

SEE PROFILE

Tailored Anatase/Brookite Nanocrystalline TiO₂. The Optimal Particle Features for Liquid- and Gas-Phase Photocatalytic Reactions

Silvia Ardizzone,^{*,†,‡} Claudia L. Bianchi,^{†,‡} Giuseppe Cappelletti,^{†,‡} Stefano Gialanella,[§] Carlo Pirola,[†] and Vittorio Ragaini[†]

Department of Physical Chemistry and Electrochemistry, University of Milan, Via Golgi 19 - 20133 Milano, Italy, Consorzio INSTM, Via Giusti 9 - 50121 Firenze, Italy, and Department of Materials Engineering and Industrial Technologies, University of Trento, 38050 Mesiano (TN), Italy

Received: May 28, 2007; In Final Form: June 29, 2007

Anatase–brookite composite nanocrystals were synthesized successfully by a controlled sol–gel reaction followed by a prolonged hydrothermal aging or by mild calcinations (300 and 450 °C). The physicochemical and photocatalytic properties of the synthesized TiO₂ composites were studied along with several commercially available nanocrystalline TiO₂ samples showing different features. Rietveld refinements of the powder X-ray diffraction pattern were used to track the brookite content systematically and to generally assess the phase composition of the different samples and their crystallite sizes. SEM, TEM, and HRTEM were used to characterize the particle morphology, size, and surface faceting. BET/BJH analyses combined with mercury porosimetry determinations were employed to characterize the surface area, porosity, and pore size distribution. The surface state of the TiO₂ samples was analyzed by XPS by studying, in detail, the region of oxygen 1s to produce the OH/O_{tot} surface ratio. The photocatalytic activity of all of the samples was tested both for degradation of NO_x in the gas phase and for the oxidation of 2-chlorophenol in the liquid phase. The different samples showed the same sequence of activity for the two reactions. The highest degradation and mineralization efficiencies were achieved in the case of samples showing smaller crystallite sizes and larger surface areas. The photocatalytic activity of the anatase–brookite composite, submitted to the hydrothermal treatment, was found to be the highest for both reactions, even greater than that of a single-phase anatase sample showing a much-larger surface area. The different contributions to the photocatalytic performance of the TiO₂ nanocrystals are critically discussed.

Introduction

A great deal of effort has been devoted, in recent years, to developing oxide semiconductor photocatalysts with high activities for environmental protection and remediation procedures such as air and water purification, water disinfection, and hazardous waste remediation.^{1–4} TiO₂ is considered to be a very-promising photocatalyst because, for several reactions, it exhibits higher activity compared with that of other semiconductors and, at the same time, it shows excellent chemical stability and nontoxicity.^{4–14}

The photocatalytic activity of titania is strongly affected by the particles' physicochemical features, with respect to both structural and morphological characteristics.⁶ Structurally, TiO₂ can crystallize in three polymorphic forms: anatase (tetragonal), rutile (tetragonal), and brookite (orthorhombic). The anatase polymorph is generally reported to show the highest photoactivity compared to the brookite or rutile polymorphs because of the low recombination rate of its photogenerated electrons and holes.^{9–10} Concerning this latter aspect, some authors^{4–6} report that the composite oxide made by two titania phases can show enhanced photocatalytic activity just because of the suppressed recombination of photogenerated electrons and holes.

The use and performance of mixed TiO₂ polymorphs in photocatalytic applications are reported to be, in their turn, strongly influenced by the final oxide microstructure.⁶

There appears to be no general agreement on the effect of the particle size on the photocatalytic activity of TiO₂. Several authors report a peak efficiency, for the given reaction, in correspondence of an optimal particle size. A few examples can be mentioned. Maira et al.¹² in the photocatalytic degradation of trichloroethylene in the gas phase with particles in the 2.3–27 nm range, found an optimum particle size of 7 nm. Also, Zhang et al.¹⁴ in the oxidation of trichloromethene reported the best efficiency for an anatase size of 11 nm. Almquist and Biswas,¹³ in the photodegradation of phenol, instead report a much larger optimal particle size in the 25–40 nm range. Furthermore, other authors report a continuous increase in the photocatalytic activity with lowering of the particle size. For example, Anpo et al.¹¹ in the hydrogenation of CH₃COH report an increase in conversion when the particle size of anatase TiO₂ decreased from 11 to 3.8 nm. Relevant to this debate are the recent results by Lin et al.:⁵ the band gap of anatase TiO₂ was observed to decrease monotonically from 3.239 to 3.173 eV when the particle size decreased from 29 to 17 nm and then to increase from 3.173 to 3.289 eV as the particle size decreased from 17 to 3.8 nm, in agreement with the red and blue shifts of the band gap reported by other researchers.^{11,15} Alternatively, their results of photocatalytic oxidation of 2-chlorophenol showed that the smaller the particle size, the faster the

* Corresponding author. Tel: +39/0250314253; fax +39/0250314300; e-mail: silvia.ardizzone@unimi.it.

[†] University of Milan.

[‡] Consorzio INSTM.

[§] University of Trento.

degradation rate. Apparently, other more-appreciable effects superimpose on the variation of the band gap. The first main effect is the continuous increase of the particle surface area with the decrease in the particle size. Another issue to be considered is the ratio between the primary and secondary particle size. This is particularly important when dealing with aqueous systems because particle aggregation is inevitable in the water environment.¹⁵ Other aspects related to the particle morphology/texture can play a relevant role in the photocatalytic activity like pore size distribution and volume.⁴

On the grounds of what is presented above, the photocatalytic response of TiO₂ crystals appears to be the result of a complex balance between the nature of the pollutant molecule and the relevant particle physicochemical features; these, in their turn, being imposed by the synthetic path adopted for the material preparation.

In recent years, a great deal of activity was dedicated, by our group, to the synthesis and characterization of nanocrystalline titania materials with tailored features. Multistep synthetic paths, always implying a growth step in solution performed either in the presence or in the absence of surfactants, have led to large-surface-area nanocrystalline TiO₂ with controlled enrichment in anatase, brookite, or rutile.^{16–19}

In this work, we report on the activity of nanocrystalline titania samples with respect to the photodegradation of pollutant molecules both in aqueous slurry (2-chlorophenol) and in the gas phase (NO_x). The same series of samples with varying phase compositions, crystallite sizes, surface areas, and textural properties are tested in liquid- and gas-phase experiments, and their activity is compared with that of commonly adopted commercial TiO₂ photocatalyst standard materials.

The direct comparison between the activity of the same catalysts in liquid- and gas-phase experiments is not reported in literature frequently; recent results by Palmisano et al.²⁰ compare the degradation of the same molecule, toluene, in either liquid- or gas-phase reactions. The comparison instead of the degradation performance of the same catalysts with respect to different reactions, in liquid and gas phases, in the authors' best knowledge, has not been reported previously in literature. For experiments performed in the liquid phase, generally the effects produced by a given catalyst on the degradation of a selected model pollutant is reported with the aim of optimizing process efficiency; in the case instead of the degradation of NO_x the largest part of the literature results pertain to commercial TiO₂ samples, while the role played by the conditions of the reaction are investigated.

Experimental Section

Sample Preparation. The preparation of TiO₂ particles, by the sol–gel technique, was performed at room temperature as follows: a solution of 0.2 mol of Ti(OC₃H₇)₄ in 50 mL of propanol was stirred for 30 min at 300 rpm. Then, 9.8 mol of Milli-Q water was added, drop by drop, fast, in order to obtain a water/alkoxide molar ratio of 49 and a water/propanol molar ratio of 15. The slurry was stirred for 90 min in order to complete the hydrolysis. The precursor was dried as a xerogel: a fraction was submitted to a hydrothermal treatment (T_{hydro}) in water (spontaneous pH, T = 60 °C, t = 500 h). No washing was performed after the aging because of the low ionic strength of the aging solutions. The remaining precursor was thermally treated either at 300 (T₃₀₀) or at 450 °C (T₄₅₀) for 6 h under an oxygen stream (9 NL/h).

Three different commercial TiO₂ powders, produced by Alfa Aesar (T_AA1, T_AA2, T_AA3) were characterized and tested in both liquid and gas-phase degradation.

Sample Characterization. Diffraction data were collected with graphite-monochromated Cu K α radiation, in the 10–80° 2 θ range, $\Delta 2\theta = 0.02^\circ$, on a Bruker AXS D8 θ/θ diffractometer. Generator settings: 40 kV, 40 mA. Slits: DS 1.0 mm; AS 1.0 mm; RS 0.2 mm. Rietveld refinement has been performed using the GSAS software suite²¹ and its graphical interface EXPGUI.²² The broadening due to the instrumental contributions was taken into account by means of a calibration performed with a standard Si powder. Components of peak broadening due to strain were not varied in the fitting procedure. The convergence was, in any case, satisfactory. The backgrounds have been subtracted using a shifted Chebyshev polynomial. The diffraction peak's profile has been fitted with a pseudo-Voigt profile function. Site occupancies and the overall isotropic thermal factors have been varied.

The average diameter of the crystallites, *d*, was estimated from the most-intense reflection (101) of the TiO₂ anatase phase using the Scherrer equation.

Specific surface areas were determined by the classical BET procedure using a Coulter SA 3100 apparatus.

Mercury porosimetry was performed with the Porosimeter 2000 Series of ThermoFisher (0–200 Mpa) on the TiO₂ powders pretreated in oven overnight to remove the residual humidity.

Scanning electron microscopy (SEM) photographs are acquired by LEO 1430.

Transmission electron microscopy (TEM) images were obtained with a Philips 400T electron microscope operating at 120 kV. High-resolution (HRTEM) observations were conducted at an accelerating voltage of 200 kV with a Jeol 2100 FS electron microscope equipped with a field-emission gun. TEM samples were prepared by spreading the powders onto a carbon-coated Cu grid, after having dispersed, using an ultrasonic bath, the sample in ethanol.

XPS spectra were obtained using an M-probe apparatus (Surface Science Instruments). The source was monochromatic Al K α radiation (1486.6 eV). A spot size of 200 $\mu\text{m} \times 750 \mu\text{m}$ and pass energy of 25 eV was used. 1s level hydrocarbon-contaminant carbon was taken as the internal reference at 284.6 eV.

Photocatalytic Experiments. 2-chlorophenol (2-CP) photodegradation experiments were performed in a photocatalytic reactor system. This bench-scale system consisted of a cylindrical Pyrex-glass (*V* = 0.4 L) jacketed cooling cell with a reflective interior surface. The system was cooled and maintained at 30 °C and at pH 5.5–6. The photon source was provided by a 500 W iron halogenide lamp (Jelosil, model HG 500) emitting in the 315–400 nm wavelength range, providing a radiation intensity of $I = 2.4 \times 10^{-5}$ einstein dm^{−3} s^{−1}. TiO₂ (at a concentration of 0.1 g dm^{−3}) nanoparticles were ultrasonicated (20 min) before the experiment was started. The target organic compound was 2-chlorophenol (2-CP) ([2-CP] = 1×10^{-3} M). The residual concentrations of the parent and intermediate compounds were measured using high-performance liquid chromatography (HPLC) (Agilent, Model HP 1100). The extent of mineralization was determined through total organic carbon (TOC) analysis using Shimadzu TOC-5000A analyzer. Blank tests, performed in the dark, showed that in the adopted experimental conditions the concentration of 2-CP remained invariant over 24 h, indicating that the molecule adsorption onto TiO₂ was negligible. Experiments performed in the absence of a photocatalyst were performed to assess the extent of direct photolysis of 2-CP.

In the photocatalytic oxidation of nitrogen oxides, immobilized particulate TiO₂ layers (ca. 0.1 g) were prepared on

glass sheets (7 cm²) by deposition from a suspension of the oxide in isopropanol. The immobilized photocatalyst was set into the Pyrex reactor (with a volume of 20 L) and irradiated with an halogenide lamp (Jelossil, model HG500) emitting in the 340–400 nm wavelength range, with a nominal power of 500 W, at room temperature. The relative humidity was kept constant in all of the runs (50%). Air, NO_x, and N₂ gas streams were mixed to obtain the desired concentration (400 ppb), introduced inside the photoreactor and the photodegradation products concentrations (NO and NO₂) were monitored continuously by an on-line chemiluminescent analyzer (Teledyne Instruments M200E). The NO_x adsorption onto the TiO₂ layer was determined through dark experiments. The degradation time was limited at 90 min because of the instrumental detection limit for NO_x concentration below 20 ppb.

Results and Discussion

TiO₂ Structural and Morphological Characterization. Of the different TiO₂ polymorphs, both the anatase and rutile phases have been largely investigated as photocatalysts, and the activity of anatase is generally considered superior to that of rutile. In contrast, there is a limited number of reports on the activity of the brookite phase. Ohtani et al.²³ reported that the brookite-type TiO₂ showed almost the same activity as anatase for the photocatalytic mineralization of acetic acid; and Kominami et al.²⁴ showed for pure brookite TiO₂, prepared by a solvothermal method, an activity comparable to that of Degussa P-25 TiO₂.

As a strategy for enhancing the charge separation to reduce charge-carrier recombination, coupling of different semiconductors can be proposed. In this work, samples composed of a mixture of anatase and brookite with an average phase enrichment ratio of 70/30 are directly synthesized by a sol–gel procedure. This specific polymorph ratio was selected on one side to allow a significantly larger anatase enrichment with respect to brookite.

In the sol–gel process, the water content determines the initial species formed during the hydrolysis and therefore strongly impacts the resultant phase produced.^{16,18,19,25} Brookite can be obtained in mixture with anatase by modulating the sol–gel conditions of the reaction. Penn et al.²⁶ report that the enrichment in brookite can be obtained by decreasing the water/alkoxide ratio (from 700:1 to 4:1) and by increasing the pH (from 0 to 9). In previous works by our group, it was noted that increasing the water/alkoxide molar ratio led to reduced crystallite size even in the calcined material.¹⁶ High water/alkoxide ratios in the reaction medium ensure a more-complete hydrolysis of alkoxides, favoring nucleation versus particle growth. The present synthesis was aimed at obtaining, on one side, the indicated enrichment in anatase and brookite and, on the other side, samples composed by small crystallites with large surface areas. Consequently, for the current reaction, an intermediate value of water/alkoxide ratio (W/A = 50) together with room-temperature conditions and neutral pH were adopted for the hydrolysis and polycondensation reactions. The gels were dried as xerogels and submitted either to a prolonged hydrothermal growth (T_{hydro}) or to mild calcination treatments (T₃₀₀ and T₄₅₀). The features of the samples prepared in the laboratory are compared with those of high-purity commercial samples with varying characteristics.

Figure 1 reports the comparison between the X-ray patterns of the investigated samples. The sol–gel samples synthesized in the laboratory are in any case composed of both the anatase and the brookite polymorphs. The substantial number of

overlapping peaks for anatase and brookite could result, by a semiquantitative approach, in significant underestimates of the brookite content in sol–gel synthesized titanium dioxide particles.²⁷ To adequately determine the relative amount of these polymorphs, we adopted the Rietveld refinement method, which, by fitting the whole X-ray diffraction pattern, varies systematically constraints to minimize differences between experimental and simulated pattern. The amount of brookite of the uncalcined hydrothermal sample and that of the sample calcined at 300 °C are very similar (see Table 1, third column). This result is in agreement with data by Penn et al.,²⁶ which show that aging the titanium dioxide particles for 8 h at 200 °C provoked no significant change in the brookite content. Heating the xerogel at 450 °C results in a slight decrease in the brookite amount. By elaborating the half width of the (101) anatase peak, by means of the Scherrer equation, the size of the crystallites of the three samples were estimated and turned out to be in any case very small, ranging from 6 to 11 nm (see Table 1, seventh column).

The three commercial samples, T_AA1, T_AA2, and T_AA3, were selected in order to present progressively varying features. The T_AA1 pattern is representative of a crystalline sample with a well-defined peak at 25.4°, identified as the 100% intensity peak of the anatase polymorph. No other reflections pertaining to other TiO₂ polymorphs are detectable. Sample T_AA2 shows instead, besides the anatase peaks, less-intense peaks pertaining to the rutile polymorph whose amount, assessed by the Rietveld refinement of the X-ray lines, can be estimated to be 9 wt % (Table 1). Sample T_AA3 is again composed of only the pure anatase polymorph. The size of the crystallites of the three commercial samples is bigger than that of the sol–gel samples and increases from 9 to 86 nm (Table 1).

The microstructural features of the powder samples were characterized further by TEM observations. Figure 2 displays the grain morphology of the six samples, and from this kind of image the crystallite sizes, d_{TEM} , in Table 1 (sixth column) were estimated. Equiaxed or, as in the case of T_AA2 specimen, spherical crystallites have been observed. Sol–gel specimens definitely display a more-homogeneous distribution of particle size. The same is true for the T_AA1 powder, whereas the other two commercial materials feature quite-broad particle size distributions. This is particularly evident in the case of the spherical particles in the T_AA2 specimen. This broader particle size distribution of the commercial powders determines higher deviations from the average values (see Table 1).

N₂ adsorption isotherms at subcritical temperatures were obtained for all samples. The adsorption of gas on a surface gives valuable information about the area and pore structure of the sample under study. Applying the BET model to the N₂ adsorption isotherms, one can calculate the specific surface area by using linear regression in the low-pressure range. The S_{BET} of all of the samples are reported in Table 1 (fifth column). The BET surface area, S_{BET} , can be written, according to the following equation, as the total surface area of the powder population divided by the powder mass²⁸

$$S_{\text{BET}} = 6 \frac{\sum_i N_i d_i^2}{\rho \sum_i N_i d_i^3} = \frac{6 \times 10^4}{\rho d_{\text{BET}}}$$

where ρ is the density of the sample (4.9 g cm⁻³). The factor 6 applies for spherical as well as for cubic particles. d_{BET} is therefore the average particle size in the assumption that both

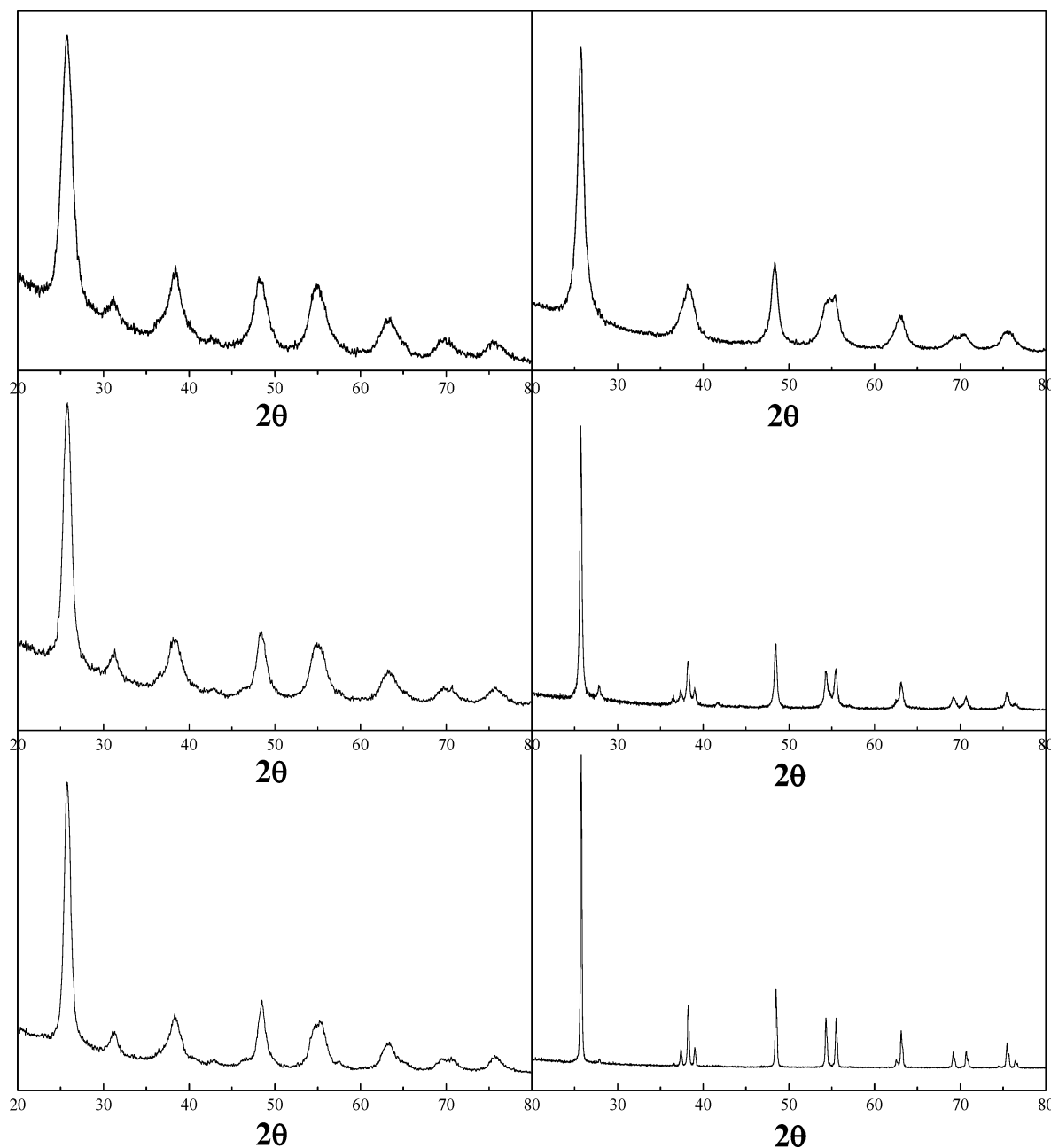


Figure 1. Powder X-ray diffraction lines of both homemade (T_hydro, T_300 and T_450) and commercial (T_AA1, T_AA2 and T_AA3) samples.

TABLE 1: Quantitative Phase Composition (A = Anatase, B = Brookite, R = Rutile); BET Surface Area; Crystallite Diameter by TEM, XRD (Scherrer Equation) and BET Measurements; Total Pore Volume

sample	% A	% B	% R	S_{BET} , m^2g^{-1}	d_{TEM} , nm	$d_{\text{XRD}}(101)$, nm	d_{BET} , nm	V_{pore} , mlg^{-1}
T_hydro	65	35		200	7 ± 2	6 ± 1	8 ± 1	0.258
T_300	68	32		145	8 ± 3	8 ± 1	11 ± 2	0.318
T_450	74	26		108	13 ± 5	11 ± 2	14 ± 3	0.263
T_AA1	100			287	7 ± 2	9 ± 1	5 ± 1	0.442
T_AA2	91		9	43	24 ± 12	35 ± 8	35 ± 6	0.369
T_AA3	100			9	134 ± 47	86 ± 18	169 ± 15	0.048

porosity and surface roughness are negligible. Table 1 reports, for all samples, the comparison among the average sizes of the crystallites as obtained from X-ray profile analysis (d_{XRD}), the size obtained by TEM (d_{TEM}), and the particle size obtained by elaboration of the specific surface area (d_{BET}). In the case of the sol-gel samples the three values are fully comparable, and for the hydrothermal sample (T_hydro) the agreement is excellent. This occurrence indicates that the particles are present mainly in the sample as single crystals with negligible aggrega-

tion or sintering. In the case of the commercial T_AA1 sample, the d_{BET} value is possibly underestimated because of the relevant porosity in the low-pore-size regime present in this sample. However, the comparability between the d_{XRD} and d_{TEM} values show that for this sample the degree of aggregation between the crystallites is also not relevant. In addition, in the case of T_AA2 the agreement between the values is good, whereas a large degree of aggregation/sintering between the crystallites is apparent for sample T_AA3.

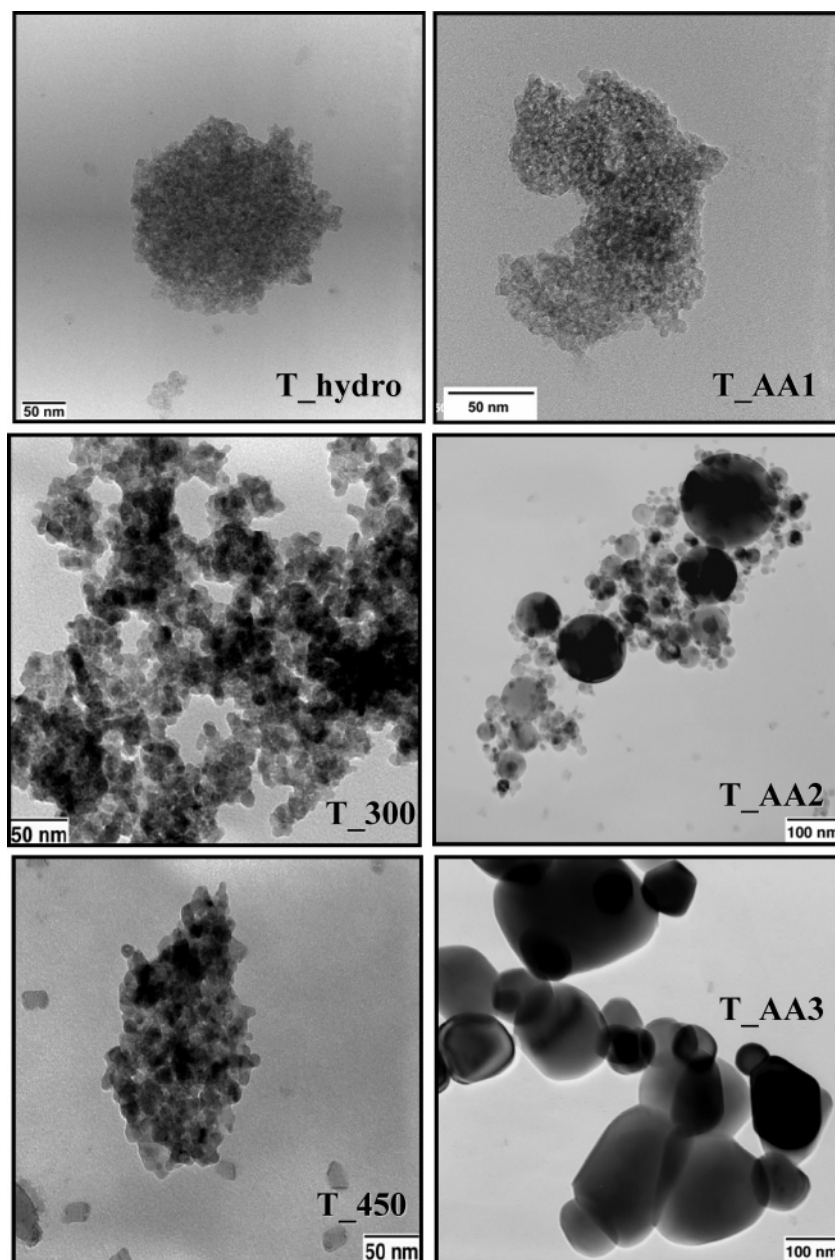


Figure 2. TEM images of homemade (T_hydro, T_300 and T_450) and commercial (T_AA1, T_AA2 and T_AA3) samples.

Photocatalytic Activity, Surface State, and Texture. Figure 3 shows the 2-CP degradation, obtained under irradiation, in the presence of a constant amount (0.1 g dm^{-3}) of the different TiO_2 samples. The figure also reports, for the sake of comparison, the curve of the reference experiment performed in the absence of TiO_2 . A kinetic modeling of the reactivity is out of the aim of the current work; however, on the grounds of the initial degradation rate, the order of magnitude of 2-CP degradation first-order kinetic constant is observed to vary in the $2.8\text{--}4.1 \times 10^{-5} \text{ s}^{-1}$ range.

The total mineralization observed at the end of the reaction, for the different samples, by TOC is summarized in Table 2. It is interesting that both conversion and total mineralization follow a comparable trend for the different samples. The overall, general trend follows an order imposed primarily by the sample crystallite size/surface area: the T_AA3 sample characterized by the largest crystallite sizes and smallest surface area shows the lowest degradation rate; the best efficiency is instead presented by the two samples showing the smallest crystallite sizes and largest surface area. These results are in agreement

with the progressive increase in 2-CP degradation with the decrease in particle size reported by Lin et al.,⁵ for pure anatase samples. Other particle features superimpose to this main effect. The T_AA2 commercial sample, for example, presents a degradation efficiency that is high if its surface area ($45 \text{ m}^2\text{g}^{-1}$) is taken into account; it should be recalled (see Table 1 and Figure 2) that this sample has some distinctive features with respect to other samples: it contains a minor amount of rutile (9%), and it shows a particular morphology (see Figure 2 and the comments to Figure 4).

The sample showing the best 2-CP degradation efficiency (and best mineralization) is the sample prepared by the sol-gel procedure and submitted to a prolonged hydrothermal growth. This sample is a mixture of anatase and brookite (A/B = 70/30), with crystallites of 6 nm and a surface area of $200 \text{ m}^2\text{g}^{-1}$. The performance of this sample is even better than that of the T_AA1 commercial sample, pure anatase, showing crystallites of comparable size (9 nm) and a surface area almost one-third larger ($287 \text{ m}^2\text{g}^{-1}$). It can be proposed that the composite (anatase/brookite) nature of the hydrothermal sample

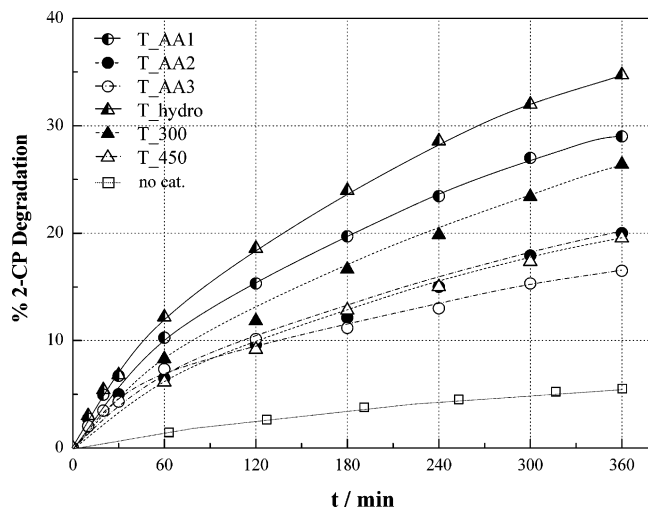


Figure 3. Liquid-phase 2-chlorophenol photodegradation for all samples: $[2\text{-CP}]^0 = 1 \times 10^{-3} \text{ M}$, $T = 30^\circ \text{C}$, $\text{pH} = 5.5 - 6$, 0.1 g/L TiO_2 . \square refer to blank experiments performed in the absence of TiO_2 .

TABLE 2: Total Organic Carbon of 2-CP Degradation at 360 min Reaction Time

sample	% degradation (TOC)
no cat.	6
T_AA1	29
T_AA2	18
T_AA3	16
T_hydro	34
T_300	22
T_450	23

plays a role in enhancing the global performance possibly by slowing recombination between electrons and holes, as suggested for the anatase/rutile composites.

Figure 4 reports the rate of NO_x degradation for the same TiO_2 photocatalysts tested in liquid-phase experiments. The figure also reports the curve representative of the TiO_2 adsorption in dark experiments. The NO_x concentration is the sum of the NO and NO_2 concentrations; the general mechanism of NO_x oxidation by photocatalysts implies the oxidation of the nitric monoxide to nitric acid or nitrous by active oxygen species produced on the TiO_2 surface.²⁹

In the present case, no increase in activity was observed by increasing the catalyst amount; consequently, it was concluded

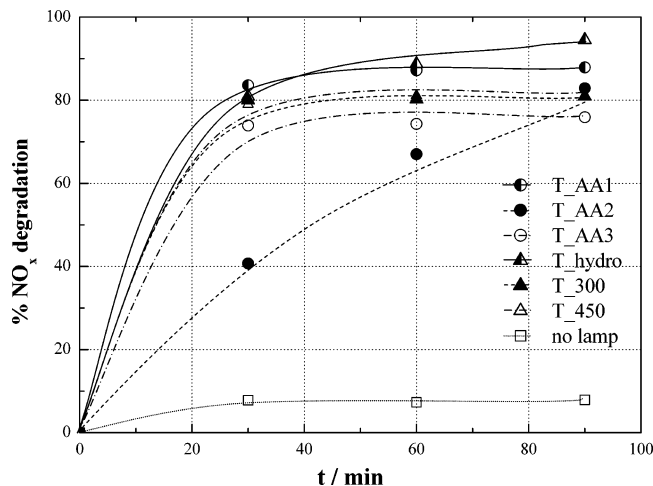


Figure 4. Gas-phase NO_x photodegradation for all samples: $[\text{NO}_x]^0 = 400 \text{ ppb}$, $T = 30^\circ \text{C}$, relative humidity = 50%, 0.1 g TiO_2 . \square refer to “dark” experiments. The reported curve is an average between the T_AA1 and T_AA3 adsorption data.

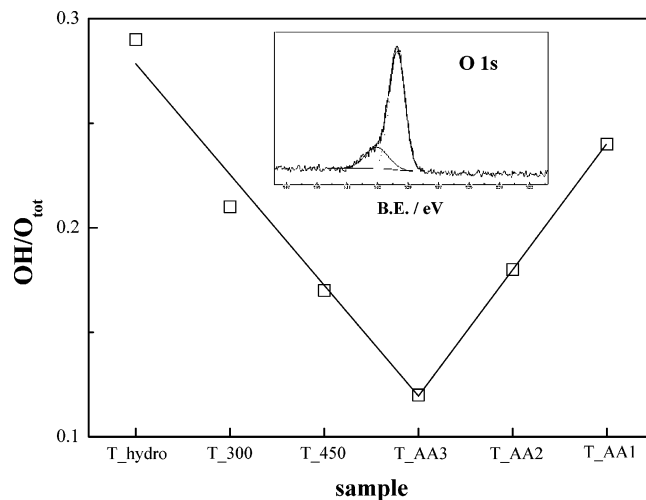


Figure 5. $\text{OH}/\text{O}_{\text{tot}}$ XPS surface ratio of the present samples. Inset: a representative O 1s peak fitting.

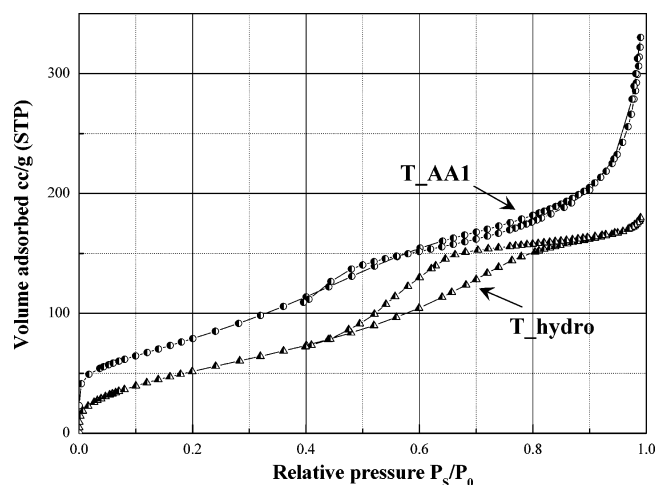


Figure 6. Comparison between BET isotherms of T_AA1 and T_hydro.

that only the exposed/external fraction of the catalyst was irradiated. All of the different samples, except sample T_AA2, show relatively high efficiencies and reach very fast (30 min) a quasi plateau region for NO_x degradations in the 75–95% range. At short reaction times, the rate of degradation of sample T_AA2 is instead much slower, whereas at 90 min the efficiency is comparable to the one of the other samples. On the grounds of the microstructural characterizations it can be proposed that, in this material, a sort of diffusion barrier is present between the working atmosphere and the active oxide. TEM observations (see TEM micrograph for T_AA2 sample in Figure 2) have, in fact, evidenced the presence of TiO_2 crystallites with a core–shell structure for this sample. This barrier-like microstructure could hinder an immediate reaction between the gaseous NO_x and titanium oxide particles.

The final sequence in efficiency, between the various samples, apparent in Figure 4, is fully comparable to that observed for the degradation of 2-CP. This result can be considered to be relevant and, at least in part, unexpected. In fact, even though, the adopted experimental parameters (radiation intensity, temperature, etc.) were identical in the two cases, the conditions of the two photocatalytic reactions are intrinsically very different; in fact, degradation of 2-CP is performed in an aqueous slurry of the oxide while in the NO_x degradation, layers of TiO_2 are immobilized onto a glass lamina and react in the gas phase. Apparently, the mediator role, played by water in the aqueous

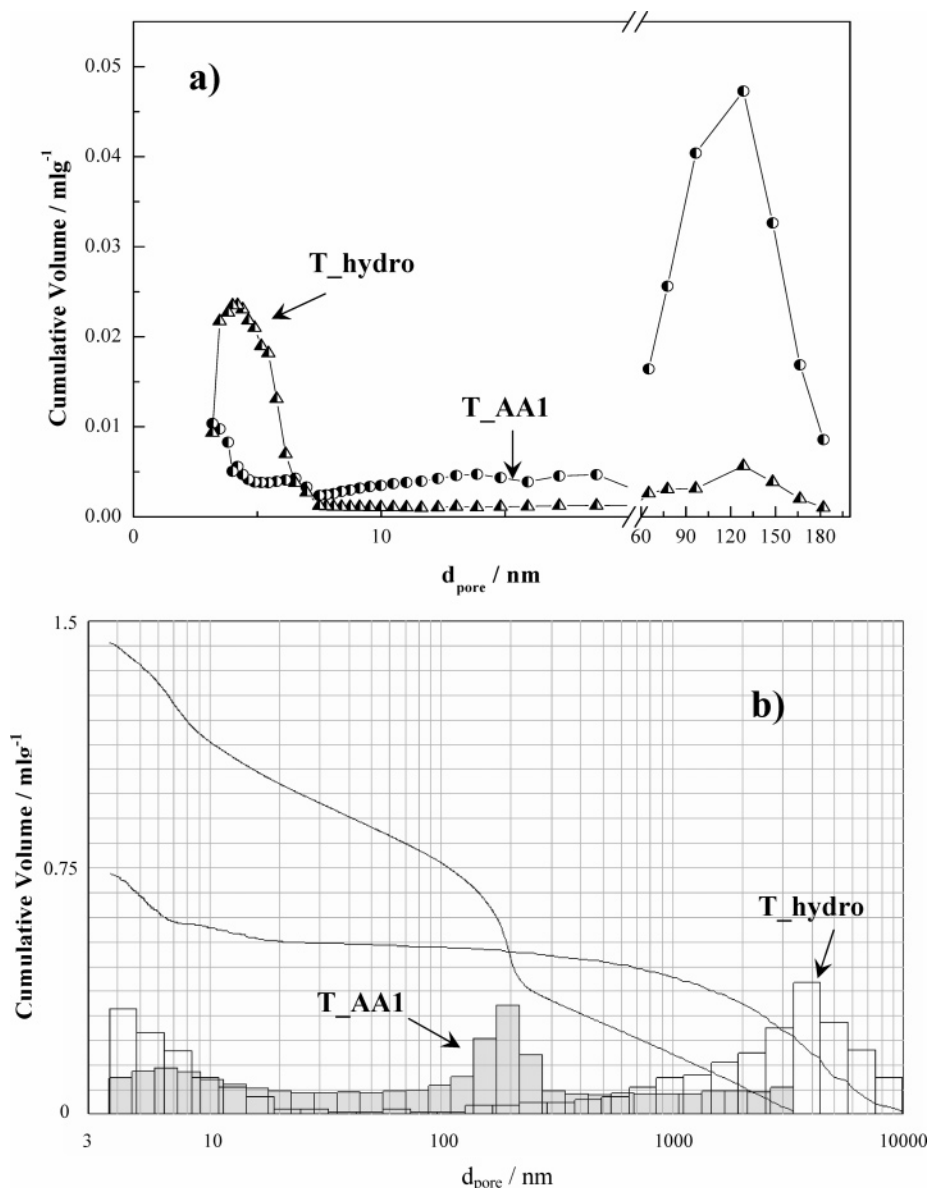


Figure 7. T_{hydro} and T_{AA1} cumulative pore volume as a function of pore diameter by the BJH method (a) and by Hg-porosimetry (b).

slurry, does not modify the photoreactivity of the samples, with respect to the conditions of the gas-phase reaction. This aspect can be very important for applications.

To obtain experimental evidence concerning the interactions between the present samples and water, XPS spectra of the oxygen 1s region were acquired for all samples.

The XPS oxygen 1s peak of oxides is, as a rule, complex and shows the presence of more than one component. The oxygen peak is generally fitted by two components, corresponding, respectively, to oxygen in the oxide lattice and surface OH groups or undissociated water.³⁰ Figure 5 reports, as an inset, a representative O 1s peak of the present samples. The best fit yields two components, which can be attributed, respectively, to lattice oxygen in TiO₂ (529.9 eV, A component) and surface OH species (531.9 eV, B component). Figure 5 reports the ratio between the surface OH and the total oxygen components for the present samples. From the trend in the figure, it is immediately apparent that the samples showing the best photocatalytic performance are the ones showing the largest OH component. This result indicates that, for both the slurry and the gas phase, the interactions with water play a relevant role in affecting the final performance. In the case of the slurry, it

might have been expected that good wetting conditions, between the particles and the solvent, may lead to a better dispersion of the particle in the medium and hence to a better reactivity. In the case of the gas phase, however, water is required as a reactant for the oxidation of NO.³¹ The product of this reaction is the OH radical that can then initiate the oxidation of NO.

As a general consideration, and also on the grounds of the data in Figure 5, it can be observed that the two samples, T_{hydro} and T_{AA1}, which present the best photocatalytic activity, show very similar physicochemical features, the main differences being the relevant presence of brookite in the sol-gel sample, which apparently makes up for the larger surface area of T_{AA1}. The textural features of the two best-performing samples will be examined in the following in more detail to highlight possible distinctive aspects between the two samples.

Figure 6 shows the nitrogen adsorption isotherms with the relative hysteresis loops for the two samples. The observed hysteresis is characteristic of a mesoporosity.³² By applying the BJH (Barrett, Joyner, Halenda) model³³ based on capillary condensation in mesopores, the mesopore size distribution can be obtained. The essential features of the hysteresis loops were explained by de Boer in terms of pore shape and the location

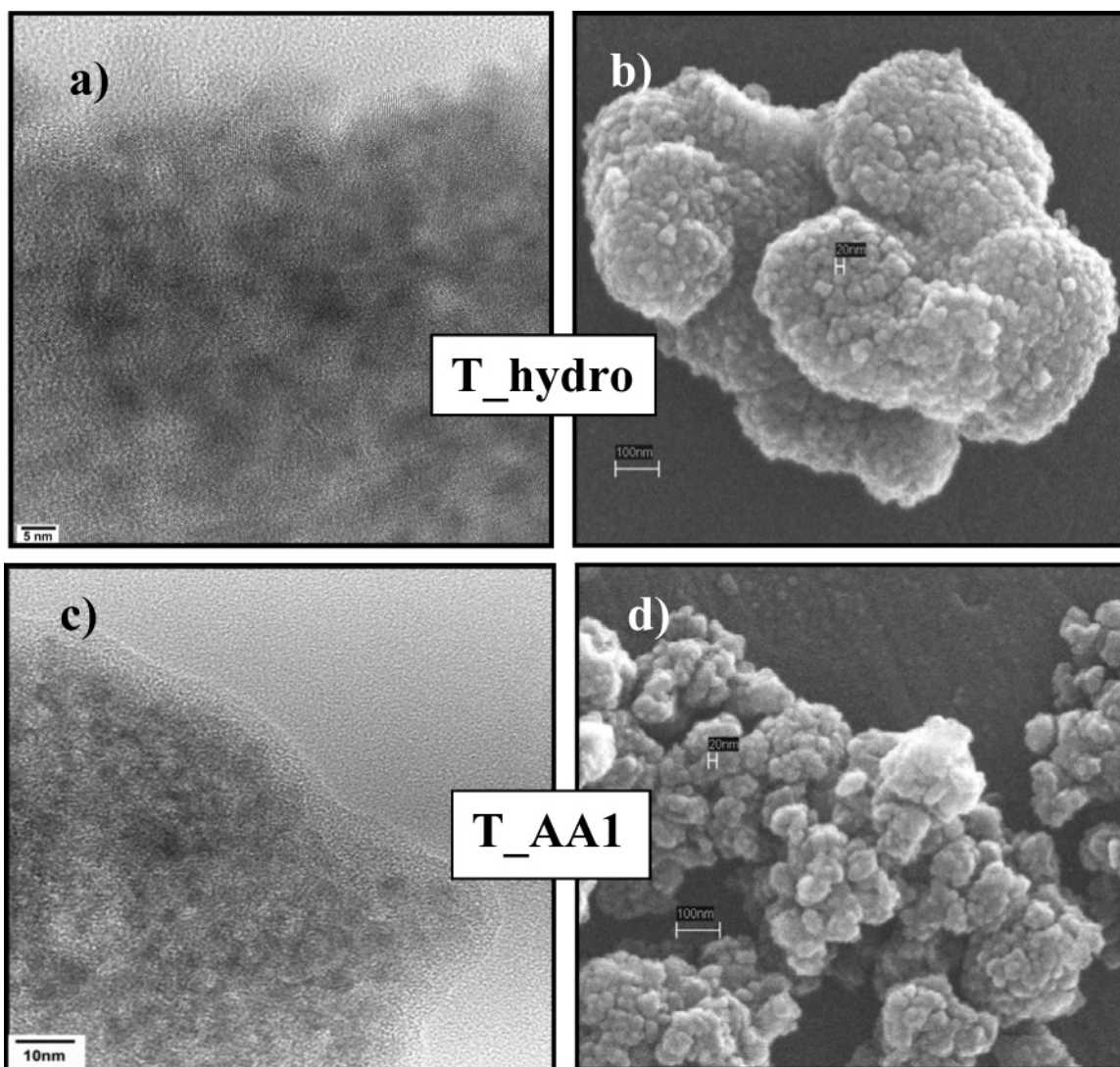


Figure 8. HRTEM and SEM images of T_{hydro} (a, b) and T_{AA1} (c, d), respectively.

and form of the liquid meniscus.³⁴ The type-B loop (sample T_{AA1}) is usually found with slit-shaped pores, in some case as the result of packing of plate-like particles, whereas the type-E hysteresis loop (sample T_{hydro}) is characterized by the steep, almost vertical, desorption branch, which follows the nearly horizontal part at high p/p° . Such loops are often associated with capillary condensation in “ink bottle” pores, that is, pore shaving narrow necks and wide bodies. Besides the shape, the size distribution of the pores is also different for the two samples. Figure 7a reports the mesopore size distribution obtained using the BJH model. For sample T_{hydro}, most of the mesopores are centered around 5 nm, whereas sample T_{AA1} shows an average pore size centered at much larger pore sizes, that is, around 130–150 nm.

The mercury porosimetry results for the two samples are shown in Figure 7b. In very good agreement with nitrogen adsorption measurements, an average pore size around 150 nm is observed in sample T_{AA1}. In the case of sample T_{hydro}, the mercury porosimetry shows, in agreement with nitrogen adsorption, a relevant porosity in the lower size range (<10 nm) but also a relevant macroporosity not measurable by nitrogen adsorption. Taking into account the TEM observations, the mesoporosity of the samples can be attributed to interparticle porosity in agglomerates (intra-agglomerate porosity). The peak at a high pore radius for sample T_{AA1} must be due to the

interagglomerate porosity, which appears distributed between 60 and 180 nm.

SEM micrographs (Figure 8a) and HRTEM images (Figure 8a,c) and SEM micrographs (Figure 8b,d) display the fine microstructure of the sol–gel prepared (T_{hydro}) and commercial (T_{AA1}) samples. The T_{hydro} powder shows the occurrence of surface faceting and of some crystallographic organization (edge, corners, etc.). In this case, instead of the T_{AA1} sample, smaller agglomerates are visible and the presence of an amorphous layer at the surface of the particles is shown clearly by the HRTEM images.

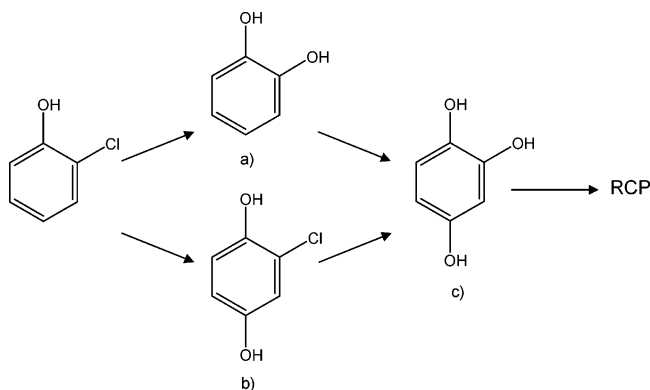
Discussion

TiO₂ photocatalysts prepared by the sol–gel procedure in the laboratory show more regular and controlled features with respect to commercial samples. The sequence of performance between the different TiO₂ samples closely corresponds in the two different photocatalytic experiments, performed, respectively, in the liquid and gas phase. As a general trend, both of the present reactions are promoted by samples showing large surface areas and small crystallites. This aspect is relevant because opposite trends are present in the literature concerning this latter aspect.

The basic species responsible for the photodegradation of pollutant molecules are hydroxyl radicals or valence band holes.

The excitation of electrons from the valence band to the conduction band, by photons, generates holes (h_{vb}) in the valence band that may either combine with hydroxyl species, adsorbed at the TiO_2 surface, to form the hydroxyl radical or directly decompose the pollutant molecule.

The degradation profile for the degradation of chlorophenol proceeds through a stepwise formation of intermediates:



Catechol (a) and chlorohydroquinone (b) are the products of the initial stages of degradation. Further reactions lead to pyrogallol (c) and finally to ring-cleavage products (RCP).

In the present conditions, catechol was the main aromatic intermediate, in agreement with literature results.^{35,36} Dekany et al.,³⁶ in studying the degradation of 2-CP, observed that aromatic intermediates, for example, chlorohydroquinone and catechol, appear in the liquid phase in the initial phase of conversion. After longer irradiation times, these aromatic intermediates undergo further photocatalytic oxidation to ring cleavage to yield carboxylic acids and aldehydes, which finally give CO_2 and H_2O due to decarboxylation. Formaldehyde is the present main side product at 360 min reaction time. The above reaction scheme supports a degradation mechanism based on the hydroxylation of reagent and intermediates by hydroxyl radicals. Sivalingam et al.³⁷ in the case of the photodegradation of substituted phenols have shown that all of the pollutants follow a mechanism based on hydroxylation by the hydroxyl radical.

The reaction path for NO_x conversion is similarly mediated by OH radicals:



Highly subdivided oxides with hydrophilic surfaces may be expected to favor OH adsorption. Consistent with this hypothesis, the present samples showing the best activity, for both chlorophenol and NO_x degradation, are actually the samples displaying the largest surface areas and the highest $\text{OH}/\text{O}_{\text{tot}}$ surface ratios.

An efficient adsorption of the pollutant molecule at the semiconductor surface may promote the photocatalytic reaction. The adsorption of chlorophenols on oxide surfaces has been shown to be a key factor in determining the subsequent photocatalytic efficiency.³⁸ Bandara et al.,^{39,40} in discussing the behavior of different photocatalysts, have shown that the degree of adsorption of 2-CP onto a given oxide surface is directly correlated to the observed degradation rates.

The adsorption of a reaction molecule is the result of a subtle balance of different effects including the polar/hydrophilic character of the molecule/substrate, solid surface charge and

state. Often, very similar pollutant molecules show opposite trends with respect to the same solid substrate. Just in the case of anatase/brookite systems, Ozawa et al.² report for the gas-phase oxidation of CH_3CHO that the crystallinity is a key factor in controlling the photocatalytic oxidation. In contrast, large surface area, that is, small crystallites, bear importance for the photocatalytic oxidation of CH_3COCH_3 in the same anatase–brookite system. In the present case, the pH (5.5–6) was selected to be in the region of the point of zero charge of TiO_2 in order to exclude adsorbate/adsorbent electrostatic interactions.

In principle, adsorbents showing large surface areas and a high density of OH groups are expected to better adsorb polar, hydrophilic molecules. 2-CP is not highly polar (dipole moment 2.88 D) and presents an intermediate hydrophobic character as attested by its value of the *n*-octanol/water partition coefficient ($\log K_{\text{o/w}} = 2.15$).⁴¹ However its adsorption at oxide surfaces is reported to be strongly favored by a high density of surface OH groups; infrared spectroscopy data show, in fact, that the adsorption of chlorophenols on oxides surfaces implies ligand exchange with surface OH groups.^{39,40}

The adsorption of NO at oxide surfaces, in the presence of oxygen, is reported to imply the formation of both surface bridged nitrates and bidentate nitrates.⁴² Therefore, also in this case a large surface area and OH population can be expected to promote the molecule adsorption.

There is a last aspect that may further account for the higher activity of T-hydro with respect to the pure anatase T-AA1. It can be suggested that the enhanced activity shown by the composite TiO_2 results from the increase in charge separation efficiency due to interfacial electron transfer via the junction between anatase and brookite nanocrystals, by analogy with what is directly shown in the anatase–rutile systems by EPR spectroscopy.⁴³ This effect is promoted further in the case of T-hydro where, because of the hydrothermal treatment, anatase and brookite crystallites are better interwoven. Furthermore, as shown by HRTEM determinations this sample is more-regular and well-faceted and can be considered to contain a relatively low concentration of defects, resulting in a lower recombination rate.

Conclusions

TiO_2 nanocrystalline anatase–brookite composites, showing an A/B ratio of 70/30, were synthesized successfully by tuning the parameters of a sol–gel reaction using Ti alkoxide as the starting compound. The sol–gel precursors were further submitted either to long hydrothermal aging or to mild calcinations. The morphological features of the sol–gel samples and particularly those of the hydrothermal sample appear to be more regular than those of nanocrystalline commercial samples used as a comparison. The different TiO_2 photocatalysts are tested with respect to the degradation of 2-CP in solution and of NO_x in the gas phase. Both reactions are promoted by samples showing large surface areas and small crystallites. Besides this general trend, other, more subtle, features promote the photoactivity in the case of the present reactions and make T_hydro, the sol–gel sample submitted to a prolonged hydrothermal growth, the best photocatalyst, even better than the pure anatase sample showing a surface area one-third larger.

A key feature appears to be the OH population of the surface: in the case of both of the present degradations, the best photocatalysts are the ones showing a large $\text{OH}/\text{O}_{\text{tot}}$ surface ratio, which apparently promotes both the formation of OH radicals and the adsorption of the pollutant molecules prior to the degradation. The presence of interwoven anatase/brookite

crystallites and limited surface defectivity as observed in the case of T-hydro promote the degradation efficiency further by reducing recombination between photogenerated electrons and holes.

Acknowledgment. This research has been supported by the Ministry of Education, University and Research (MIUR, FIRST Funds).

References and Notes

- (1) Mills, A.; Hunte, S. L. *J. Photochem. Photobiol.* **1997**, *A* 108, 1.
- (2) Ozawa, T.; Iwasaki, M.; Tada, H.; Akita, T.; Tanaka, K.; Ito, S. *J. Colloid Interface Sci.* **2005**, *281*, 510–513.
- (3) Hu, C.; Wang, Y. Z.; Tang, H. X. *Chemosphere* **2000**, *41*, 1205.
- (4) Yu, J.; Yu, J. C.; Leung, M. K.-P.; Cheng, W.; Ho, B.; Zhao, X.; Zhao, J. *J. Catal.* **2003**, *217*, 69–78.
- (5) Lin, H.; Huang, C. P.; Li, W.; Ni, C.; Ismat Shah, S.; Tseng, Y.-H. *Appl. Catal., B* **2006**, *68*, 1–11.
- (6) Bakardjieva, S.; Stengl, V.; Szatmary, L.; Subrt, J.; Lukac, J.; Murafa, N.; Niznansky, D.; Cizek, K.; Jirkovskyc, J.; Petrova, N. *J. Mater. Chem.* **2006**, *16*, 1709–1716.
- (7) Kolar, M.; Mest'ankova, H.; Jirkovsky, J.; Heyrovsky, M.; Subrt, J. *Langmuir* **2006**, *22*, 598–604.
- (8) Krysa, J.; Jirkovsky, J. *J. Appl. Electrochem.* **2002**, *32*, 591–596.
- (9) Yanagisawa, K.; Ovenstone, J. *J. Phys. Chem.* **1999**, *B* 103, 7781.
- (10) Fujishima, A.; Rao, T. N.; Tryk, D. A. *J. Photochem. Photobiol.* **2000**, *C* 1, 1.
- (11) Anpo, M.; Shima, T.; Kodama, S.; Kubokawa, Y. *J. Phys. Chem.* **1987**, *91*, 4305–4310.
- (12) Maira, A. J.; Yeung, K. L.; Lee, C. Y.; Yeu, P. L.; Chan, C. K. *J. Catal.* **2000**, *192*, 185–196.
- (13) Almquist, C. B.; Biswas, P. *J. Catal.* **2002**, *212*, 145–156.
- (14) Zhang, Z.; Wang, C. C.; Zakaria, R.; Ying, J. Y. *J. Phys. Chem. B* **1998**, *102*, 10871–10878.
- (15) Kormann, C.; Bahnemann, D. W.; Hoffmann, M. R. *J. Phys. Chem.* **1988**, *92*, 5196–5201.
- (16) Boiadjieva, T.; Cappelletti, G.; Ardizzzone, S.; Rondinini, S.; Vertova, A. *PCCP* **2004**, *6*, 3535–3539.
- (17) Bianchi, C. L.; Ardizzzone, S.; Cappelletti, G. In *Dekker Encyclopedia of Nanoscience and Nanotechnology*; Dekker: New York, 2006; pp 1–10 (DOI: 10.1081/E-ENN-120042107).
- (18) Cappelletti, G.; Bianchi, C. L.; Ardizzzone, S. *Appl. Surf. Sci.* **2006**, *253*, 519–524.
- (19) Ardizzzone, S.; Bianchi, C. L.; Cappelletti, G. *Surf. Interface Anal.* **2006**, *38*, 452–457.
- (20) Marcì, G.; Addamo, M.; Agugliaro, V.; Coluccia, S.; Garcia-Lopez, E.; Loddò, V.; Martra, G.; Palmisano, L.; Schiavello, M. *J. Photochem. Photobiol., A* **2003**, *160*, 105–114.
- (21) Larson, A. C.; Von Dreele, R. B. *GSAS: General Structural Analysis System*; Los Alamos National Laboratory: Los Alamos, NM, 1994.
- (22) Toby, B. H. *J. Appl. Crystallogr.* **2001**, *34*, 210.
- (23) Ohtani, B.; Handa, J.; Nishimoto, S.; Kagiya, T. *Chem. Phys. Lett.* **1985**, *120*, 292.
- (24) Kominami, H.; Ishii, Y.; Kohno, M.; Konishi, S.; Kera, Y.; Ohtani, B. *Catal. Lett.* **2003**, *91*, 41–47.
- (25) Li, Y.; White, T. J.; Lim, S. H. *J. Solid State Chem.* **2004**, *177*, 1372.
- (26) Isley, S. L.; Penn, R. L. *J. Phys. Chem. B* **2006**, *110*, 15134–15139.
- (27) Zhang, H.; Finnegan, M.; Banfield, J. F. *Nano Lett.* **2001**, *1*, 81.
- (28) Weibel, A.; Bouchet, R.; Boulc'h, F.; Knauth, P. *Chem. Mater.* **2005**, *17*, 2378–2385.
- (29) Tseng, Y.-H.; Kuo, C.-S.; Huang, C.-H.; Li, Y.-Y.; Chou, P.-W.; Cheng, C.-L.; Wong, M.-S. *Nanotechnology* **2006**, *17*, 2490–2497.
- (30) Crist, B. V. *Handbook of Monochromatic XPS Spectra: The Elements and Native Oxides*, Wiley: Chichester, 2000; pp 279–282.
- (31) Wang, H.; Wu, Z.; Zhao, W.; Guan, B. *Chemosphere* **2007**, *66*, 185–190.
- (32) Rouquerol, J.; Rouquerol, F.; Sing, K. S. W. In *Adsorption by Powders and Porous Solids*; Academic Press: London, 1999.
- (33) Barrett, E. P.; Joyner, L. G.; Halenda, P. H. *J. Am. Chem. Soc.* **1951**, *73*, 373.
- (34) de Boer, J. H.; Lippens, B. C.; Linsen, B. G.; Broekhof, J. C. P.; van den Heuvel, A.; Osinga, Th. J. *J. Colloid. Interface. Sci.* **1966**, *21*, 405.
- (35) Bertelli, M.; Selli, E. *J. Hazard. Mater.* **2006**, *B138*, 46–52.
- (36) Mogyorosi, K.; Farkas, A.; Dekany, I.; Ilisz, I.; Dombi, A. *Environ. Sci. Technol.* **2002**, *36*, 3618–3624.
- (37) Sivalingam, G.; Priya, M. H.; Madras, G. *Appl. Catal., B* **2004**, *51*, 67–76.
- (38) Cunningham, J.; Sayyed, G. *J. Chem. Soc., Faraday Trans.* **1990**, *86*, 3941.
- (39) Bandara, J.; Mielczarski, J. A.; Kiwi, J. *Appl. Catal., B* **2001**, *34*, 307–320.
- (40) Bandara, J.; Mielczarski, J. A.; Lopez, A.; Kiwi, J. *Appl. Catal., B* **2001**, *34*, 321–333.
- (41) Liu, G.; Yu, J. *Water Res.* **2005**, *39*, 2048–2055.
- (42) Tsyntarski, B.; Avreyska, V.; Kolev, H.; Marinova, Ts.; Klissurski, D.; Hadjiivanov, K. *J. Mol. Catal., A* **2003**, *193*, 139–149.
- (43) Hurum, D.; Agrios, A. A.; Gray, K. A.; Rajh, T.; Thurnauer, M. C. *J. Phys. Chem. B* **2003**, *107*, 4545–4549.